Crustal and uppermost mantle shear velocity structure adjacent to the Juan de Fuca Ridge from ambient seismic noise

Ye Tian, Weisen Shen, and Michael H. Ritzwoller

Center for Imaging the Earth's Interior, Department of Physics, University of Colorado at Boulder, Boulder, Colorado, 80309, USA (Ye.Tian@colorado.edu)

[1] Based on 6 months of OBS data from the Cascadia Initiative experiment near the Juan de Fuca Ridge, we obtain Rayleigh wave group and phase speed curves from 6 s to about 20 s period from ambient noise cross correlations among all station pairs. We confirm the hypothesis that the dispersion data can be fit by a simple age-dependent formula, which we invert using a Bayesian Monte Carlo formalism for an age-dependent shear wave speed model of the crust and uppermost mantle between crustal ages of 0.5 and 3.5 Ma. Igneous crustal structure is age invariant with a thickness of 7 km, water depth varies in a prescribed way, and sedimentary thickness and mantle shear wave speeds are found to increase systematically with crustal age. The mantle model possesses a shallow low shear velocity zone (LVZ) with a velocity minimum at about 20 km depth at 0.5 Ma with lithosphere thickening monotonically with age. Minimum mantle shear velocities at young ages are lower than predicted from a half-space conductively cooling model (HSCM) and the lithosphere thickens with age faster than the HSCM, providing evidence for nonconductive cooling in the young lithosphere. The shallow LVZ is consistent with expectations for a largely dehydrated depleted (harzburgite) mantle with a small, retained near-ridge partial melt fraction probably less than 1% with melt extending to a lithospheric age of approximately 1 Ma (i.e., ∼30 km from the ridge).

1. Introduction

[2] Seismic information on the early evolution of the oceanic mantle lithosphere near spreading ridges has been derived principally from the MELT and Gravity Lineations, Intraplate Melting, Petrologic and Seismic Expedition (GLIMPSE) experiments [e.g., *MELT Seismic Team*, 1998; *Harmon et al.*, 2009; *Yao et al.*, 2011] near the East Pacific Rise (EPR), a fast spreading ridge with a full spreading rate of about 14 cm/yr. The recent deployment of ocean bottom seismographs

(OBS) by the Cascadia Initiative on the Juan de Fuca Plate and the open availability of these data provide the opportunity to characterize the mantle lithosphere near a slower spreading ridge (∼6 cm/ yr) and ultimately to extend analyses to the entire plate. *Harmon et al*. [2007] and *Yao et al*. [2011] showed that short period Rayleigh waves and the first higher mode can be observed using cross correlations of ambient noise recorded on OBS installed near the EPR. They used these waves to constrain shear wave speeds in the oceanic crust and uppermost mantle. Here, we analyze cross correlations of the first 6 months of ambient noise recorded by OBS installed near the Juan de Fuca ridge in order to determine shear wave speeds in the crust and uppermost mantle in the young Juan de Fuca plate to an age of about 3.5 Ma (i.e., to distances up to about 100 km from the ridge crest).

[3] Our goal is to reveal the age-dependent structure of the shallow oceanic lithosphere in the young Juan de Fuca plate in order to illuminate the physical processes at work there. In particular, we are interested in modeling the accumulation of sediments and the variation of shear wave speeds in the uppermost mantle to a depth of about 60 km. Like *Harmon et al*. [2009] for the region near the EPR, we compare the estimated mantle shear wave speeds with those predicted from a conductively cooling half-space to test for the presence of non-conducting cooling processes (e.g., convection, fluid advection, lateral heat flux). In addition, we compare with the more sophisticated physical model of *Goes et al*. [2012] in order to investigate whether dissolved water or interstitial partial melt are present. *Goes et al*. [2012] argue for a double low shear velocity zone (LVZ) with a shallow LVZ between about 20 and 50 km depth caused by dry (or damp) partial melting near to the spreading ridge and a deeper LVZ between about 60 and 150 km caused by solid-state anelasticity, where low Q values result from dissolved water. Our model, however, extends only to a depth of 60 km and provides no information about a deeper LVZ.

2. Methods

2.1. Data Processing

[4] The Cascadia Initiative (CI) experiment provides the OBS data for this study based on instruments from three different contributors: SIO, LDEO, and WHOI. Because the CI team discovered a (subsequently corrected) timing error that affected the SIO data, we focus attention on the WHOI data near the Juan de Fuca Ridge. This restricts analysis to 23 stations. Stations G03A, G30A, and J06A are outside of the study area and are, therefore, not used and the vertical channel of station J48A failed during the deployment. We analyze only the long period (1 sps) channel at each station, which eliminates station J61A and restricts our analysis to Rayleigh waves above about 6 s period. Figure 1a shows the study area and the 18 stations used, 15 of which are located to the east of the Juan de Fuca ridge and provide path coverage up to about 200 km into the Juan de Fuca plate. Approximately 6 months of continuous data are available for most of these stations. When we downloaded the data, horizontal components had not yet been rotated into the east-west and north-south directions. Therefore, we do not use horizontal data, but restrict analysis to the vertical components (and therefore Rayleigh waves).

[5] We computed ambient noise cross correlations between the vertical components of all stations by applying traditional ambient noise data processing (time domain normalization, frequency domain normalization) to produce the empirical Green's functions [*Bensen et al*., 2007]. An example of an empirical Green's function between stations J47A and J29A (Figure 1b) is shown in Figure 1c. The Rayleigh waveforms are highly dispersed and display two Airy phases such that the short-period phase (representative of the water-sediment waveguide) arrives far after the longer period phase (representative of the igneous crust and uppermost mantle waveguide). Frequency-time analysis [e.g., *Levshin and Ritzwoller*, 2001; *Bensen et al*., 2007] is applied to the symmetric component (average of positive and negative correlation lags) of each cross correlation to measure Rayleigh wave group and phase speeds between periods of about 6 and 20 s. Longer periods require longer time series lengths and may be obtainable as more data become available. An example frequency-time analysis (FTAN) diagram is presented in Figure 1d showing both the Rayleigh wave group and phase speed curves. Rayleigh wave group speeds range from about 1 km/s at the short period end to more than 3.6 km/s at longer periods and phase speeds range from about 1.8 km/s to more than 3.6 km/s. At periods below 6 s the phase and group speed curves would approach each other asymptotically, but are separate in the observed period band. *Harmon et al*. [2007] and *Yao et al*. [2011] observed the first higher mode below 6 s period, which cannot be observed with the long period data used in our study. Paths that are mainly to the west of the
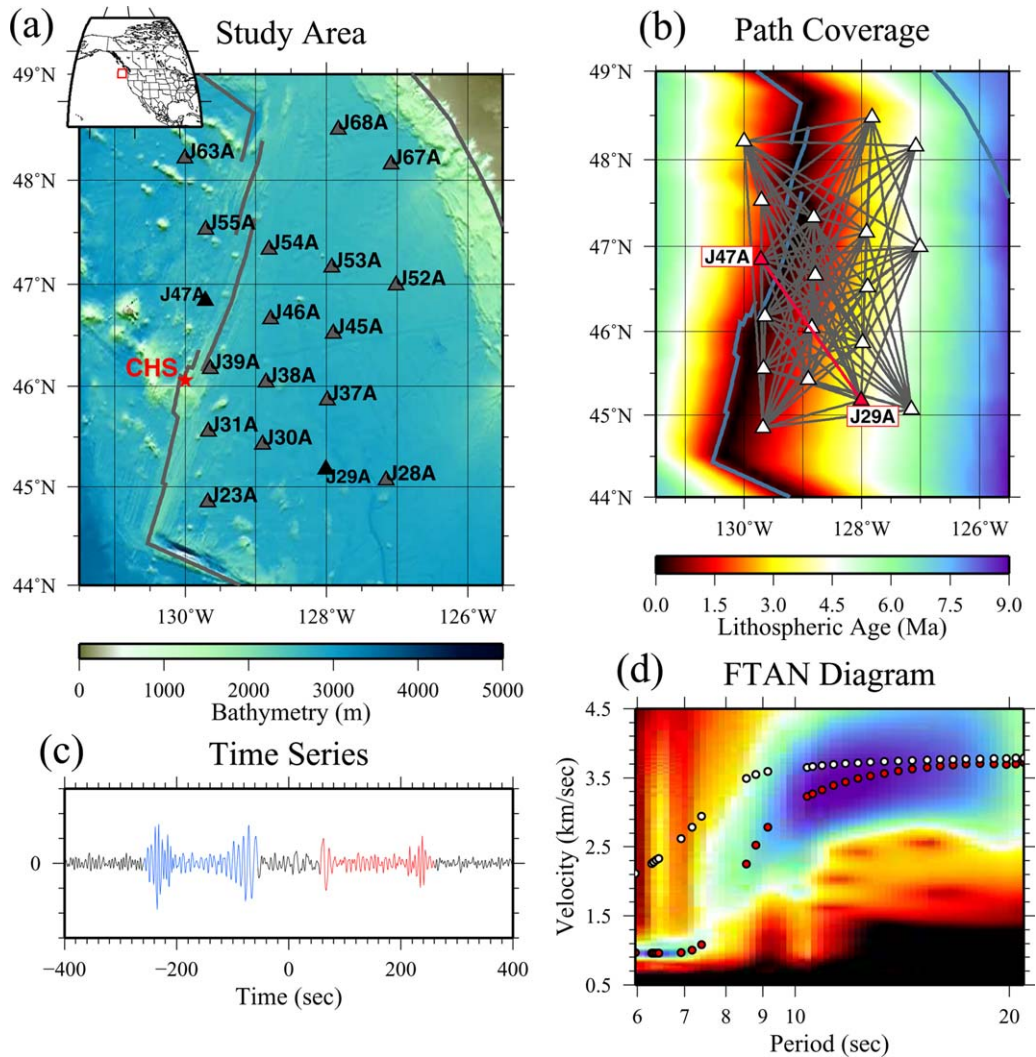
Figure 1. (a) The locations of the 18 long period Cascadia Initiative OBS stations used in this study (triangles) are plotted over bathymetry with the Juan de Fuca Ridge shown as the gray line. The red star (denoted CHS) marks the approximate location of the Cobb hot spot. (b) The 106 interstation ray paths are plotted with gray lines over lithospheric age [*Mueller et al.*, 1997]. (c) Example 6 month cross correlation for data from stations J29A and J47A, marked as red triangles bounding the red interstation path in Figure 1b. The waveform is colored red or blue for the positive or negative correlation lag with group speeds corresponding to the fundamental mode. (d) Rayleigh wave velocity versus period (FTAN) diagram of the symmetric component of the signal shown in Figure 1c. Background color indicates the spectral amplitude and group and phase speeds are shown with red and white circles, respectively.

ridge are discarded because they reflect the structure of the Pacific plate and may be more affected by the Cobb hotspot (Figure 1a). Dispersion measurements for paths shorter than three wavelengths are also discarded. As discussed in the following paragraph, data are also selected based on signal-to-noise ratio (SNR) and the agreement of dispersion measurements obtained on the positive and negative lag components of the cross correlations. Finally, a total of 106 interstation paths are accepted and plotted in Figure 1b.

[6] As a measure of measurement uncertainty and to search for possible timing errors, we compare phase speed measurements obtained from the positive and negative lag components of the cross correlations. Not all cross correlations have arrivals on both lags, but 65 of the 106 interstation measurements have a signal-to-noise ratio (SNR) greater than 5 on both lags at 14 s period, which allows for the comparison of interlag travel times shown in Figure 2a. We make the assumption that the interlag travel time differences are normally
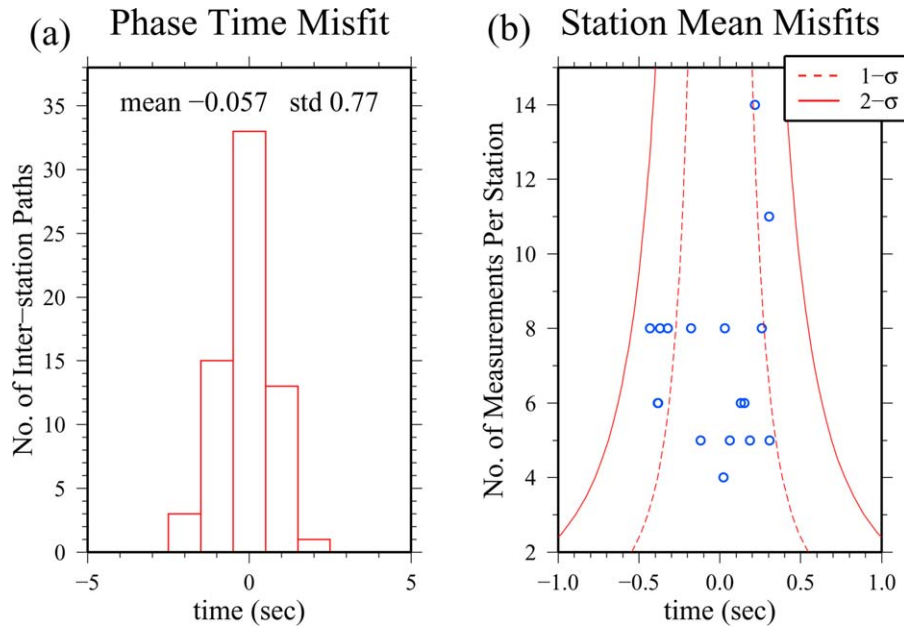
Figure 2. (a) Estimate of measurement error. The histogram shows the distribution of the differences between measurements of positive and negative lag interstation phase times for the 14 s Rayleigh wave (mean = −0.057 s, std dev = 0.77 s is taken as measurement error). (b) Nondetection of a timing error. Each dot is the mean time difference for a particular station between the positive and negative lags (associated with outgoing and incoming waves) for the 14 s Rayleigh wave. Red dashed and solid lines indicate the 1 and 2 standard deviation confidence intervals, respectively. No mean difference is outside of the 2 standard deviation confidence interval.

distributed and estimate the standard deviation of the entire population to be 0.77 s from the standard deviation of the travel time differences of the 65 interstation paths. For these 65 interstation measurements, if the discrepancy between the positive and negative lag phase times (or more accurately, times of outgoing and incoming waves) is less than 1% we average the positive and negative lag cross correlations (forming the symmetric signal) and measure group and phase velocities using the resulting signal. For the remaining interstation measurements, we use only the lag with the higher SNR and retain the measurement if the SNR on that lag is greater than 5. The comparison between phase travel times on the positive and negative lags can also be used to detect timing errors [e.g., *Stehly et al.*, 2007; *Lin et al.*, 2007]. Figure 2b presents the mean difference for each station between the measurements of outgoing and incoming phase times at 14 s period. The 1 and 2 standard deviation intervals are computed based on the estimated population standard deviation and the number of measurements for each station. As seen in Figure 2b, the measurement means are all within the 2 standard deviation interval and no station displays an absolute difference in the mean larger than 0.5 s. This is interpreted as evidence that there is no

differential timing error amongst the data that we use in this study, which all come from WHOI.

[7] The resulting path coverage (Figure 1b) is not ideal to produce Rayleigh wave group or phase speed maps using either traditional tomographic methods [e.g., *Barmin et al.*, 2001] or eikonal tomography [*Lin et al.*, 2009]. For this reason, we proceed by testing the hypothesis that Rayleigh wave phase and group speeds depend principally on lithospheric age. At each period, we follow *Harmon et al.* [2009] and test a velocity-age relationship of the following form:

$$v = c_0 + c_1\sqrt{a} + c_2 a \qquad (1)$$

where v represents either the observed interstation Rayleigh wave group or phase velocity, a represents the seafloor age in millions of years (Ma), and c_0, c_1, and c_2 are period-dependent unknowns that differ for phase and group speeds and which we attempt to estimate.

[8] For each measurement type (phase or group) and each period extending discretely from 6 to 20 s, we estimate the three coefficients c_0, c_1, and c_2. The wave travel time along a path is given by the following path integral, which occurs over a path
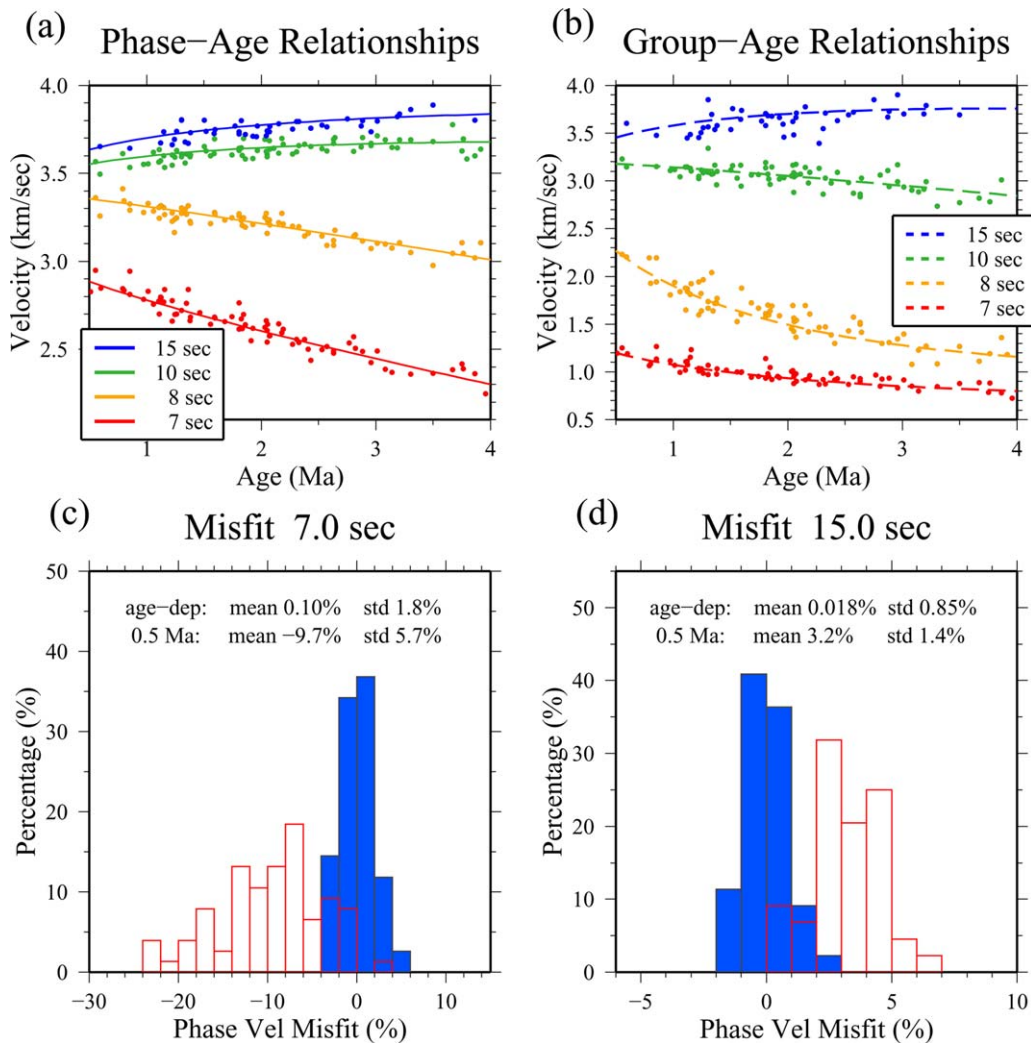
Figure 3. (a) Solid lines are the estimated age-dependent Rayleigh wave phase velocities (equation (1)) at 7 (red), 8 (orange), 10 (green), and 15 (blue) s period. Colored dots are the measured interstation phase velocities plotted at the average of the lithospheric age along the interstation path. (b) Same as Figure 3a, but for Rayleigh wave group velocities at the same periods. Blue histograms are the misfit (in percent) to the observed interstation phase velocities at (c) 7 and (d) 15 s period produced by the estimated age-dependent phase speed curves (equation (1)). At 7 s and 15 s period, respectively, mean misfits are 0.1% and 0.02% and the standard deviations of the misfits are 1.8% and 0.9%. The red histograms are the misfits based on the 0.5 Ma model. At 7 and 15 s period, respectively, mean misfits from this age-independent model are −9.7% and 3.2% and the standard deviations of the misfits are 5.7% and 1.4%. Thus, the age-dependent model significantly reduces the standard deviation of the misfit compared with an age-independent model and produces a nearly zero-mean misfit.

whose dependence on crustal age is prescribed by the lithospheric age model of *Mueller et al.* [1997] shown in Figure 1b:

$$t_{path} = \sum_{path} \frac{ds}{c_0 + c_1\sqrt{a} + c_2 a} \quad (2)$$

[9] To determine the set of best fitting coefficients at each period, we perform a grid search to minimize the total squared misfit:

$$\sum_i \left(\frac{S_i^{path}}{t_i^{path}} - v_i^{path} \right)^2, \quad (3)$$

where S_i^{path}, t_i^{path}, and v_i^{path} are the interstation path length, the predicted travel time for a particular choice of c_0, c_1, and c_2, and the observed wave speed for the ith path, respectively.

[10] Figures 3a and 3b summarize the resulting estimates of Rayleigh wave phase and group velocity

versus lithospheric age at periods of 7, 8, 10, and 15 s. At short periods, velocities decrease with age because water depth and sedimentary thickness increase. At longer periods, they increase with age because they are sensitive to the cooling mantle. In Figures 3a and 3b, in order to illustrate the fit to the data we overplot the estimated velocity-age curves with the interstation observations presented at the average of the lithospheric ages of the two stations. The simple velocity versus age curves given by equation (1) capture the trend in these interstation group and phase speed measurements, although associating each measurement with a single lithospheric age is not entirely appropriate. An F test shows that the square root term is only important at periods longer than about 9 s, while the linear term is, in general, important at periods below 14 s. This is expected because the shorter periods are controlled mainly by the linear thickening of the combination of water and sediments, whereas the longer periods are primarily sensitive to mantle thermal structures which change approximately proportionally to the square root of lithospheric age.

[11] Fully accurate phase velocity misfit (blue) histograms at 7 and 15 s period are presented in Figures 3c and 3d for the age-dependent model, with the standard deviation (std) of misfit of about 1.8% and 0.9%, respectively, and mean misfits less than 0.1%. These values represent a large improvement compared to any age-independent model. For example, the misfit using our estimated phase speed model at 0.5 Ma is presented in Figures 3c and 3d with the red histograms. The one standard deviation misfit using this model is 5.7% and 1.4% at 7 and 15 s period, respectively, with mean misfits of −9.7% and 3.2%. Because group velocity is a more difficult observable with larger uncertainties than phase velocity, the final misfit is higher but is still substantially better than any age-independent model. Our age-dependent model neglects azimuthal anisotropy. However, we did estimate azimuthal anisotropy at all periods and found that the expected bias in isotropic shear wave speed is less than about 0.3% at all periods, which is within estimated uncertainties.

[12] In conclusion, the fit to the observations by the Rayleigh wave phase velocity versus age model presented by equation (1) is sufficient to base further interpretation exclusively on the age dependence of the group and phase velocities. Although other spatially dependent variations in Rayleigh wave speeds are expected to exist (and are interesting in their own right), they can be ignored safely in our analysis, which aims to produce an age-
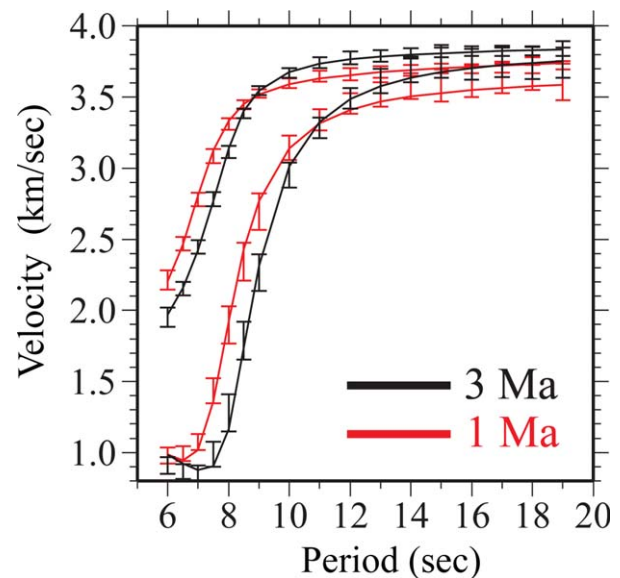
Figure 4. Estimated dispersion curves for seafloor ages of 1 Ma (red) and 3 Ma (black). Error bars are the measured Rayleigh wave phase velocity and the estimated 1 standard deviation uncertainty. Solid curves are the predictions from the inverted age-dependent shear velocity model (Figure 6).

dependent model for the crust and uppermost mantle for the young Juan de Fuca plate. The final result of the data analysis is a set of age-dependent Rayleigh wave phase and group velocity curves such as those at 1 and 3 Ma shown in Figure 4. The error bars are the one standard deviation misfits to the observations given by the estimated age-dependent curves such as those shown in Figures 3a and 3b.

2.2. Bayesian Monte Carlo Inversion

[13] Examples of the data and uncertainties at 1 and 3 Ma are presented in Figure 4. We are particularly interested in interpreting the age dependence of such curves, which is affected by water depth, sedimentary thickness, crustal thickness, uppermost mantle shear wave speeds, and anelasticity. The shear velocity model we produce is actually a Vsv model because it derives exclusively from Rayleigh waves.

2.2.1. Parameterization and Constraints
[14] At each age, our model is composed of four layers. (1) The top layer is water with a depth that is averaged over the study area as a function of crustal age using a global bathymetry database [*Amante and Eakins*, 2009] in which Vs is set 0 km/s and Vp is 1.45 km/s. (2) The second layer comprises the sediments with a constant shear wave speed of 1 km/s [*Sun*, 2000] but with a thickness that varies with age. (3) The igneous crust
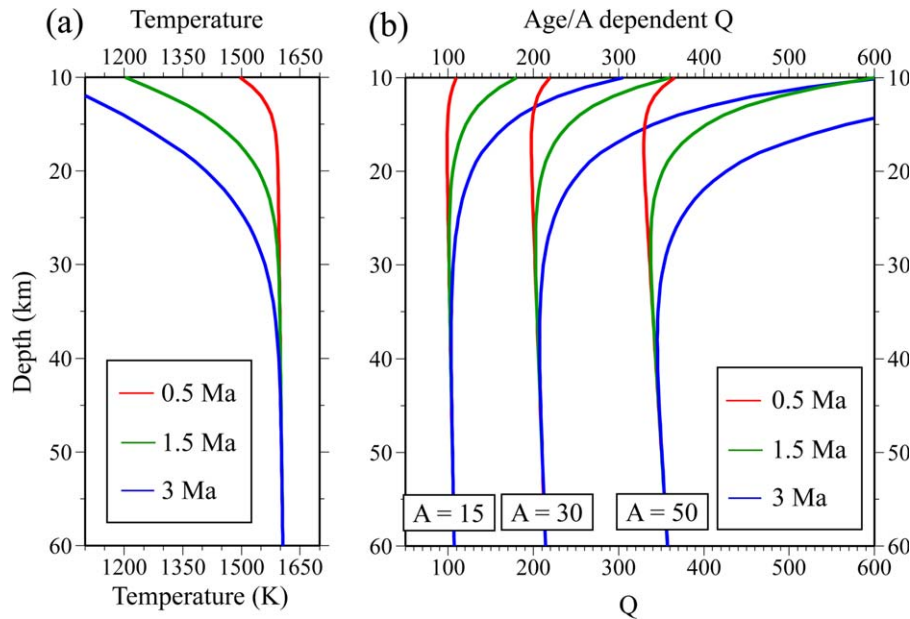
Figure 5. (a) Examples of the mantle temperatures from the half-space conductive cooling model (HSCM) plotted for three lithospheric ages. This temperature model is used in the Q-model (equation (4)). (b) Examples of Q_μ for three different lithospheric ages for three different values of the A coefficient of equation (4).

underlies the sediments and is parameterized by four cubic B-splines. (4) Finally, there is an uppermost mantle layer parameterized by three cubic B-splines from Moho to a depth of 80 km. At its base, the mantle layer is continuous with an underlying layer from the half-space conductive cooling model (HSCM) described in section 3. In the inversion, only four unknowns are age dependent: sedimentary thickness and the top three cubic B-spline coefficients in the mantle. The other parameters are set to be constant over age. Igneous crustal thickness is set constant at 7 km [e.g., *White et al.*, 1992; *Carbotte et al.*, 2008]. Crustal Vs is fixed based on an initial inversion of the 2 Ma dispersion data. Fixing the igneous crust as a function of age is consistent with gravity and multichannel seismic data along the ridge [*Marjanović et al.*, 2011] at long spatial wavelengths. The Vp/Vs ratio in the igneous crust is set to be 1.76 (consistent with PREM) and is 2.0 in the sediments. An additional prior constraint is imposed that the velocity gradient (dVs/dz) is negative directly below Moho. In the mantle, Vp is scaled from Vs with a Vp/Vs ratio of 1.76 and density is scaled from Vp using results from *Karato* [1993]. This choice has little effect on the results of the inversion.

2.2.2. Q Model

[15] Shear wave speeds in the mantle are affected both by temperature and anelasticity. The inver-

sion for a seismic model, therefore, requires the assumption of a shear Q-model. For the crust, we set Q_μ to be consistent with PREM such that it is 80 in the sediments and 600 in the igneous crust. For the mantle, the principal observations of Q_μ for young oceanic lithosphere (near the East Pacific Rise) were obtained by *Yang et al.* [2007]. The center of their period band is about 40 s, where they estimated Q_μ to lie between about 150 and 250 at depths ranging from about 10–40 km, with Q_μ decreasing at greater depths. We follow *Shapiro and Ritzwoller* [2004] (and many others) and use a temperature and frequency-dependent shear Q model of the following form:

$$Q(\omega) = A\omega^\alpha \exp\left(\alpha(E + PV)/RT\right) \qquad (4)$$

where ω is frequency in rad/s, R is the gas constant, P is pressure, T is temperature from the half-space cooling model (Figure 5a) described later, and activation volume $V = 1.0 \times 10^{-5}$ m³/mol. We set $\alpha = 0.1$ and activation energy $E = 2.5 \times 10^5$ J/mol, which are lower values than used by Shapiro et al. but more consistent with those in the study of *Harmon et al.* [2009]. In the shallow mantle, E is larger than PV so that temperature effects on Q dominate over pressure effects. Thus, what matters is the product αE, with larger values accentuating the dependence on temperature. Larger values of α or E would tend to raise Q more in the lithosphere relative to the underlying asthenosphere. Because

mantle temperatures are not well known, we choose parameters in equation (4) to make the effect of temperature relatively weak. In any event, as Figure 5a shows, age-dependent temperature differences are important only above about 25 km depth in the half-space cooling model.

[16] Inserting these values into equation (4), $A \approx$ 30 would be consistent with *Yang et al.* [2007] and *Harmon et al.* [2009], producing $Q_\mu \approx 175$ at 30 km depth at 40 s period. With this value of A, Q_μ at 10 s period (near the center of our frequency band) is plotted in Figure 5b. Three lithospheric ages are shown, using the three temperature profiles of Figure 5a, which shows that temperature effects on Q are important mostly in the top 20 km. Below 30 km depth, Q_μ is largely age-independent and equal to about 200 for $A = 30$. It is the Q model with $A = 30$ that we use in producing the mantle model presented later in the paper.

[17] The coefficient A controls the depth-averaged Q-value in the mantle. Physically, A will decrease by reducing grain size or increasing dissolved water content or retained interstitial partial melt fraction [e.g., *Faul et al.*, 2004; *Faul and Jackson*, 2005; *Behn et al.*, 2009; *Goes et al.*, 2012]. Setting $A = 15$ or $A = 50$, produces a discrete offset in Q below 30 km to about 100 or 350, respectively, as Figure 5b shows. The choice of A is probably more important in determining the Vs model than the choice of the temperature model or the other parameters in equation (4). We return later to consider the effect on the final mantle Vs model of changing A from 30 to both 15 and 50 and, therefore, depth-averaged Q_μ from 200 to 100 and 350.

[18] We present the final model at 1 s period, extrapolating from the period band of inversion using the physical dispersion correction of *Minster and Anderson* [1981].

2.2.3. The Prior Distribution

[19] The inversion is performed using a Bayesian Monte Carlo formalism, which has been described in detail and applied systematically to EarthScope USArray data by *Shen et al.* [2013a, 2013b]. An input model that defines the prior distribution is initially computed by performing an inversion with the dispersion curves at 2 Ma in which we allow the coefficients of the crustal B-splines to vary. The igneous crust for all ages is fixed at the result of this inversion. The forward problem is computed using the code of Herrmann (http://www.eas.slu.edu/eqc/eqccps.html). The best fitting model at 2 Ma (M_0) is then used to construct the model space for the age-dependent inversion.

The model space defining the prior distribution at each age is generated as follows. The sedimentary layer thickness is allowed to vary $\pm 100\%$ relative to M_0. The top first, second, and third cubic B-splines in the mantle are allowed to vary by $\pm 4\%$, $\pm 2\%$, and $\pm 1\%$, respectively, relative to M_0, which acts to squeeze heterogeneity toward shallow depth. The models at all ages reach the same deep asymptotic value at 80 km depth, which is continuous with the HSCM. Models are accepted into the posterior distribution or rejected according to the square root of the reduced χ^2 value. A model m is accepted if $\chi(m) < \chi_{min} + 0.5$, where χ_{min} is the χ value of the best fitting model. After this, the mean and standard deviation of the posterior distribution at each age are computed at each depth, where the mean is the model we present (e.g., Figure 6), and twice the standard deviation is interpreted as model uncertainty.

2.2.4. Results

[20] We estimate 1-D Vsv models from the mean of the posterior distribution using the dispersion curves at crustal ages of 0.5, 1.0, 1.5, 2.0, 2.5, 3.0, and 3.5 Ma. The major products are an age-independent igneous crust with a thickness of 7 km, a constant Vs sedimentary layer with age-variable thickness, and age-dependent Vsv as a function of depth in the uppermost mantle. Water depth and sedimentary thickness as a function of age are presented in Figure 6a. Sediments are estimated to increase in thickness from about 100 m at 0.5 Ma to about 400 m at 3.5 Ma, and the depth to the top of the igneous crust increases approximately linearly with age by about 500 m between 0.5 and 3.5 Ma. This is consistent with results from multichannel seismic (MCS) data [*Carbotte et al.*, 2008]. The age-independent igneous crustal model is presented in Figure 6b. The mantle age-dependent shear velocity profiles appear in Figure 6c. Shear wave speeds increase with age monotonically and converge by about 60 km depth below which we have little resolution. Age-dependent posterior distributions at depths of 20 and 40 km (Figures 6d and 6e) illustrate the model uncertainties and show the separation of the ensemble of accepted models at different ages. The posterior distributions reflect both prior information and the Rayleigh wave phase velocity data, however, and their narrowness in part reflects the tight constraints provided by the prior information. Still, the final age-dependent model fits the data very well, as Figure 4 illustrates. The introduction of other variables in the inversion is not justified by the need to fit the observations.
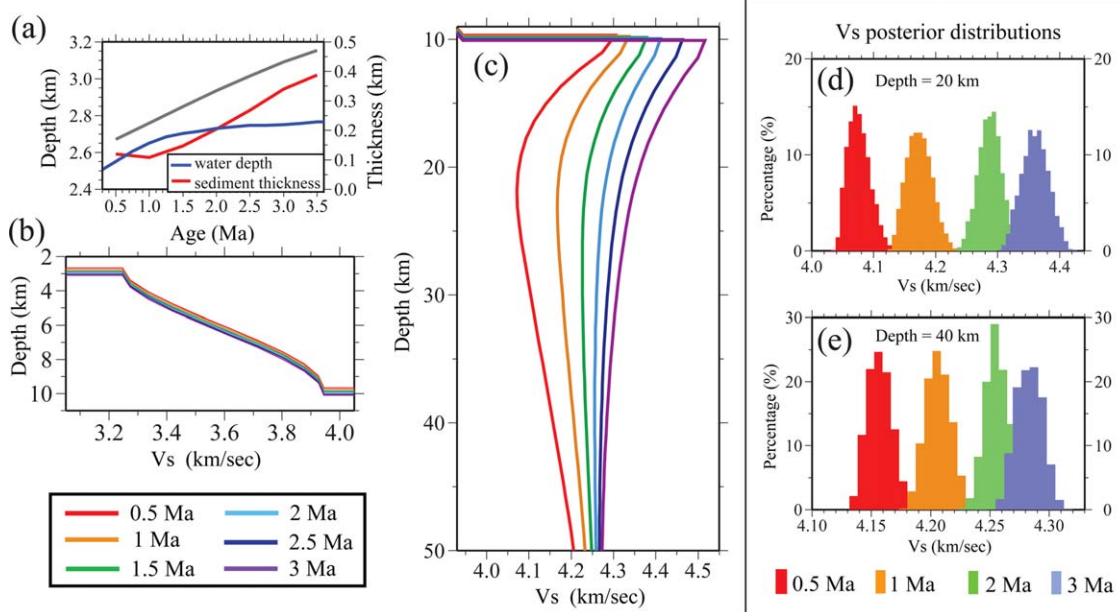
Figure 6. Estimated model. (a) Water depth (blue line), estimated sedimentary layer thickness (red line), and the estimated depth of crystalline basement below the ocean surface (gray line), which is the sum of water depth and sedimentary layer thickness. (b) Estimated crustal Vs model, which varies in age only by sediment thickness and water depth. (c) The estimated age-dependent shear wave velocity models (Vsv) in the mantle from 0.5 to 3 Ma. The mean of the estimated posterior distribution is shown for each age. The age legend at lower left corresponds both to Figures 6b and 6c. (d) Posterior distributions of Vsv models for each seafloor age at 20 km depth. (e) Same as in Figure 6d, but for 40 km depth. All models are presented at 1 s period.

[21] A LVZ in the uppermost mantle between 15 and 40 km depth is most pronounced at young crustal ages. Unfortunately, due to a shortage of paths along the ridge we are unable to provide information for lithospheric ages younger than about 0.5 Ma. At the youngest age (0.5 Ma) in our study, the minimum Vsv reaches ~4.07 km/s at 20 km depth. With uncertainties defined as the standard deviation of the posterior distribution at each depth (e.g., Figures 6d and 6e), at 20 km depth Vsv increases from 4.07 ± 0.02 km/s at 0.5 Ma to 4.37 ± 0.02 km/s at 3 Ma. At 40 km depth, Vsv increases from 4.16 ± 0.01 km/s at 0.5 Ma to 4.28 ± 0.01 km/s at 3 Ma. At greater depths both the age variation and uncertainties reduce because prior constraints strengthen.

[22] As discussed above, the choice of the shear Q-model will affect the estimated shear velocity model in the mantle. Figure 7 quantifies the effect of choosing $A = 15$, 30, or 50 in equation (4), or Q values equal to about 100, 200, or 350 below 30 km depth (with somewhat higher values in the shallower mantle arising from cooler temperatures). Lowering mantle Q increases Vs in the estimated model, but this range of Q models produces Vs models within the model uncertainty. Thus, the

choice of the Q model amongst these alternatives will not affect the conclusions reached in this paper. Much lower Q values at young lithospheric ages, as advocated for example by *Faul and Jackson* [2005], would further increase Vs in the shallow mantle. If such low Q values were to exist, however, they would probably result from partial melt. In section 3, we invoke the existence of partial melt near the ridge in order to explain the low shallow shear wave speeds we observe near the ridge crest. Thus, whether we explain the observations with low shear wave speeds (as we prefer) or exceptionally low Q near the ridge crest, partial melt would be inferred in either case.

3. Discussion and Conclusions

[23] The age-dependent mantle Vsv model is summarized in Figure 8a, which also presents the distance to the Juan de Fuca ridge (converted from age by using a half spreading rate of ~30 km/Ma [*Wilson*, 1993]). This 2-D plot is contoured with solid or dashed lines every 0.05 km/s with solid lines at shear wave speeds of 4.2, 4.3, 4.4, and 4.5 km/s and dashed lines at 4.15, 4.25, 4.35, and
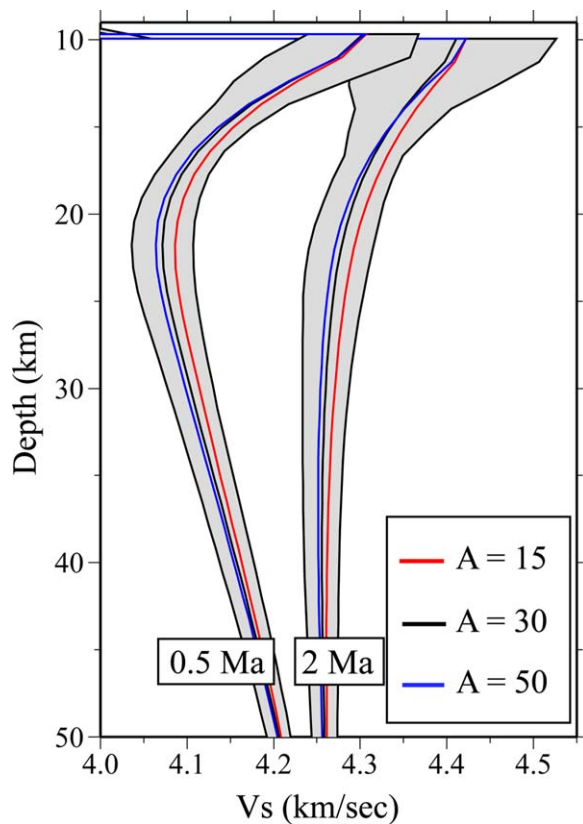
Figure 7. Effect of varying the Q model on estimates of Vs in the mantle. Vs models determined using three different Q models with varying *A* values (equation (4)) are shown: *A* = 15 (red), 30 (black), and 50 (blue). We use *A* = 30 in this paper, and the estimated two standard deviation uncertainty in the resulting model is shown with the gray corridor.

4.45 km/s. This model is compared with shear velocities converted from the thermal half-space conductively cooling model (HSCM) in Figure 8b. Temperature profiles of the HSCM at several ages are plotted in Figure 5a. In constructing the HSCM [*Turcotte and Schubert*, 2002], we use a mantle potential temperature of 1315°C and a thermal diffusivity of 10^{-6} m²/s, convert to anharmonic Vs using the approximation of *Stixrude and Lithgow-Bertelloni* [2005], and model the effect of anelasticity using the correction of *Minster and Anderson* [1981] based on the shear Q model of equation (4) with *A* = 30. The Vs model from the HSCM is presented at 1 s period to match the observed model. The predicted shear wave speed from the HSCM is isotropic Vs, whereas the model inferred from Rayleigh wave dispersion is Vsv. Knowledge of radial anisotropy in the upper mantle would allow for a correction between these values, but without Love waves we do not even know the relative sizes of Vsv and Vsh. However,

ıVsv − Vshı is probably less than 3% [*Ekstrom and Dziewonski*, 1998], and may be much smaller [e.g., *Dunn and Forsyth*, 2003; *Harmon et al.*, 2009] in the shallow mantle near the ridge, so the effect on Vs is almost certainly within ±1% assuming a Voigt-average of Vsv and Vsh. If this value were constant across the study region and we were to use it to convert the estimated Vsv to Vs in Figure 8a, the transformation would shift the mean at each depth but not the variation with age. Thus, the estimated age variation is expected to be robust relative to the introduction of radial anisotropy into the model.

[24] As observed in Figures 8a and 8b, both the estimated model and the HSCM model possess a monotonically thickening high-velocity lid at shallow mantle depths, and both have similar average shear wave speeds in the upper mantle of ~4.25 km/s. There are also prominent differences between them.

[25] 1. First, the fast lid is observed to thicken at a faster rate than for the HSCM. If we define the base of the lid (or the base of the lithosphere) to be at 4.3 km/s, then by about 3.5 Ma (~100 km from the ridge) the estimated lid thickens to ~40 km but the lid in the HSCM only penetrates to less than 30 km depth. Although the choice of 4.3 km/s is ad hoc, the observed lithospheric lid is probably more than 1.3 times thicker than predicted by the HSCM. The faster development of the lithospheric lid than predicted by the HSCM may imply non-conductive cooling processes, such as convection or the vertical advection of fluids in the shallow mantle.

[26] 2. A second major difference is that the estimated model possesses a prominent low shear velocity zone (LVZ) in the uppermost mantle (15–40 km) at young ages near the ridge (age < 1.5 Ma), but such low wave speeds are not present in the HSCM. Low shear velocities in the mantle (<4.1 km/s) at 15–40 km beneath the ridge also have been seen beneath the East Pacific Rise [*Dunn and Forsyth*, 2003; *Yao et al.*, 2011], which was attributed to partial melt beneath the ridge.

[27] Using physically more sophisticated models than the HSCM, *Goes et al.* [2012] show that if the upper mantle is depleted in basalt, resulting in a harzburgite composition of the residue, but retains dissolved water, then Vs would be far lower than what we observe in the uppermost mantle near the Juan de Fuca ridge. However, with a largely dehydrated dry or merely damp depleted mantle devoid of partial melt, no LVZ appears and
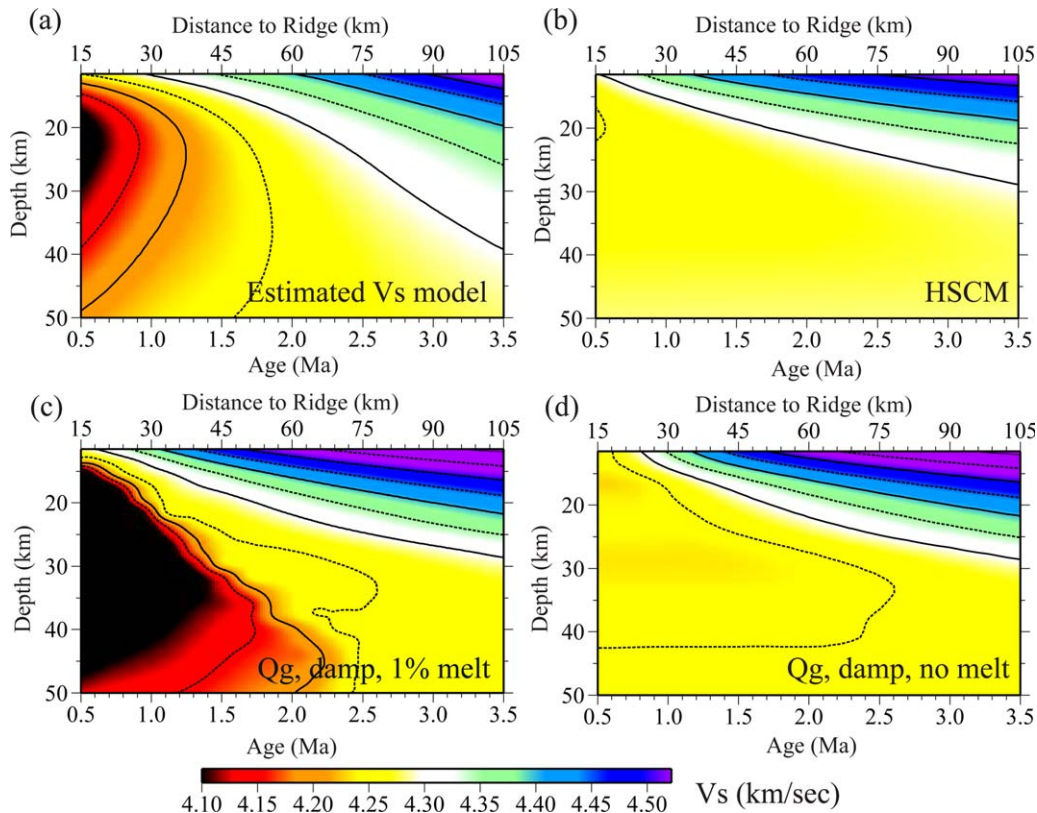
Figure 8. Comparison of (a) our estimated Vsv model and (b) the half-space conductive cooling model (HSCM) as a function of seafloor age. For further comparison, models from *Goes et al.* [2012] are presented (c) with and (d) without retained melt, respectively. Shear wave speeds in increments of 0.1 km/s are contoured with solid lines and values in odd multiples of 0.05 km/s are contoured with dashed lines. All models are converted to 1 s period for comparison. (S. Goes provided the models in Figures 8c and 8d and converted them to 1 s period self-consistently).

Vs is very similar to the HSCM as can be seen in Figure 8d. The principal difference between this model and the HSCM is more rapid cooling in the shallow mantle and the development of a thicker lid. This difference arises principally because Goes et al. include the effects of convection. They also use a more sophisticated PT-velocity conversion, which may also have contributed to the difference.

[28] In contrast Goes et al. have also included a retained partial melt fraction with a maximum of about 1%. Using the Q_g model defined in their paper, they produce the Vs model shown in Figure 8c, which displays a shallow low shear velocity zone between 10 and 50 km depth that is qualitatively similar to our model but with minimum shear velocities that are lower and with low shear velocities extending farther from the ridge. However, they take their partial derivatives of anharmonic Vs relative to a melt fraction from the highest values of *Hammond and Humphreys*

[2000] and, therefore, may have overpredicted the effect of partial melt on Vs. Still, our results are probably consistent with a retained melt fraction somewhat smaller than 1%, although this value is poorly determined.

[29] These observations lead us to conclude that the low shear wave speeds that we observe near the Juan de Fuca Ridge probably derive from a small retained melt fraction less than about 1% in a largely dry depleted harzburgitic uppermost mantle. In addition, the amplitude of the observed LVZ diminishes with age, which is consistent with cooling and the reduction in the melt fraction. By 1.0–1.5 Ma, the velocity minimum at about 20 km has largely disappeared, which, following the interpretation presented here, would probably mean that partial melt is largely absent past about 1.0 Ma (i.e., 30 km from the ridge crest).

[30] This study was performed with only 6 months of OBS data acquired near the Juan de Fuca ridge.

Since the study's completion, longer time series have been accruing and other data have become available including higher sampling rates, horizontal components, and stations nearer to the continent. Further analysis of these data as well as the assimilation of other types of data (e.g., receiver functions, heat flow measurements, etc.) are expected to extend the present study considerably.

Acknowledgments

References

Amante, C., and B. W. Eakins (2009), ETOPO1 1 Arc-Minute Global Relief Model: Procedures, data sources and analysis, NOAA Tech. Memo., NESDIS NGDC-24, 19 pp., NOAA, Available at: http://www.ngdc.noaa.gov/mgg/global.

Barmin, M. P., M. H. Ritzwoller, and A. L. Levshin (2001), A fast and reliable method for surface wave tomography, *Pure Appl. Geophys.*, *158*(8), 1351–1375, doi:10.1007/PL00001225.

Behn, M. D., G. Hirth, and J. R. Elsenbeck II (2009), Implications of grain size evolution on the seismic structure of the oceanic upper mantle, *Earth Planet. Sci. Lett.*, *282*, 178–189, doi:10.1016/j.epsl.2009.03.014.

Bensen, G. D., M. H. Ritzwoller, M. P. Barmin, A. L. Levshin, F. Lin, M. P. Moschetti, N. M. Shapiro, and Y. Yang (2007), Processing seismic ambient noise data to obtain reliable broad-band surface wave dispersion measurements, *Geophys. J. Int.*, *169*, 1239–1260, doi:10.1111/j.1365-246X.2007.03374.x.

Carbotte, S. M., M. R. Nedimović, J. P. Canales, G. M. Kent, A. J. Harding, and M. Marjanović (2008), Variable crustal structure along the Juan de Fuca Ridge: Influence of on-axis hot spots and absolute plate motions, *Geochem. Geophys. Geosyst.*, *9*, Q08001, doi:10.1029/2007GC001922.

Dunn, R. A., and D. W. Forsyth (2003), Imaging the transition between the region of mantle melt generation and the crustal magma chamber beneath the southern East Pacific Rise with short-period Love waves, *J. Geophys. Res.*, *108*(B7), 2352, doi:10.1029/2002JB002217.

Ekstrom, G., and A. M. Dziewonski (1998), The unique anisotropy of the Pacific upper mantle, *Nature*, *394*(6689), 168–172, doi:10.1038/28148.

Faul, U. H., and I. Jackson (2005), The seismological signature of temperature and grain size variations in the upper mantle, *Earth Planet. Sci. Lett.*, *234*(1–2), 119–134, doi:10.1016/j.epsl.2005.02.008.

Faul, U. H., J. D. Fitz Gerald, and I. Jackson (2004), Shear wave attenuation and dispersion in melt-bearing olivine polycrystals: 2. Microstructural interpretation and seismological implications, *J. Geophys. Res.*, *109*, B06202, doi:10.1029/2003JB002407.

Goes, S., J. Armitrage, N. Harmon, H. Smith, and R. Huismans (2012), Low seismic velocities below mid-ocean ridges: Attenuation versus melt retention, *J. Geophys. Res.*, *117*, B12403, doi:10.1029/2012JB009637.

Hammond, W. C., and E. D. Humphreys (2000), Upper mantle seismic wave velocity: Effects of realistic partial melt geometries, *J. Geophys. Res.*, *105*, 10,975–10,986.

Harmon, N., D. Forsyth, and S. Webb (2007), Using ambient seismic noise to determine short-period phase velocities and shallow shear velocities in young oceanic lithosphere, *Bull. Seismol. Soc. Am.*, *97*(6), 2009–2023, doi:10.1785/0120070050.

Harmon, N., D. W. Forsyth, and D. S. Weeraratne (2009), Thickening of young Pacific lithosphere from high-resolution Rayleigh wave tomography: A test of the conductive cooling model, *Earth Planet. Sci. Lett.*, *278*, 96–106, doi:10.1016/j.epsl.2008.11.025.

Karato, S. (1993), Importance of anelasticity in the interpretation of seismic tomography, *Geophys. Res. Lett.*, *20*(15), 1623–1626, doi:10.1029/93GL01767.

Levshin, A. L., and M. H. Ritzwoller (2001), Automated detection, extraction, and measurement of regional surface waves, *Pure Appl. Geophys.*, *158*(8), 1531–1545.

Lin, F., M. H. Ritzwoller, J. Townend, M. Savage, and S. Bannister (2007), Ambient noise Rayleigh wave tomography of New Zealand, *Geophys. J. Int.*, *170*, 649–666, doi:10.1111/j.1365-246X.2007.03414.x.

Lin, F.-C., M. H. Ritzwoller, and R. Snieder (2009), Eikonal tomography: Surface wave tomography by phase front tracking across a regional broad-band seismic array, *Geophys. J. Int.*, *177*(3), 1091–1110, doi:10.1111/j.1365-246X.2009.04105.x.

Marjanović, M., S. M. Carbotte, M. R. Nedimović, and J. P. Canales (2011), Gravity and seismic study of crustal structure along the Juan de Fuca Ridge axis and across pseudo-faults on the ridge flanks, *Geochem. Geophys. Geosyst.*, *12*, Q05008, doi:10.1029/2010GC003439.

MELT Seismic Team, (1998), Imaging the deep seismic structure beneath a mid-ocean ridge: The MELT experiment, *Science*, *280*, 1215–1218, doi:10.1126/science.280.5367.1215.

Minster, J. B., and D. L. Anderson (1981), A model of dislocation-controlled rheology for the mantle, *Philos. Trans. R. Soc. London*, *299*, 319–356.

Mueller, R. D., W. R. Roest, J.-Y. Royer, L. M. Gahagan, and J. G. Sclater (1997), Digital isochrons of the world's ocean floor, *J. Geophys. Res.*, *102*, 3211–3214.

Shapiro, N. M., and M. H. Ritzwoller (2004), Thermodynamic constraints on seismic inversions, *Geophys. J. Int.*, *157*, 1175–1188, doi:10.1111/j.1365-246X.2004.02254.x.

Shen, W., M. H. Ritzwoller, V. Schulte-Pelkum, and F.-C. Lin (2013a), Joint inversion of surface wave dispersion and receiver functions: A Bayesian Monte-Carlo approach, *Geophys. J. Int.*, *192*, 807–836, doi:10.1093/gji/ggs050.

Shen, W., M. H. Ritzwoller, and V. Schulte-Pelkum (2013b), A 3-D model of the crust and uppermost mantle beneath the central and western US by joint inversion of receiver functions and surface wave dispersion, *J. Geophys. Res.*, *118*, 1–15, doi:10.1029/2012JB009602.

Stehly, L., M. Campillo, and N. M. Shapiro (2007), Travel time measurements from noise correlations: Stability and detection of instrumental errors, *Geophys. J. Int.*, *171*, 223–230, doi:10.1111/j.1365-246X.2007.03492.x.

Stixrude, L., and C. Lithgow-Bertelloni (2005), Mineralogy and elasticity of the oceanic upper mantle: Origin of the low-velocity zone, *J. Geophys. Res.*, *110*, B03204, doi:10.1029/2004JB002965.

Sun, Y. F. (2000), Core-log-seismic integration in hemipelagic marine sediments on the eastern flank of the Juan de Fuca Ridge, *Proc. Ocean Drill. Program Sci. Results*, *168*, 21–35.

Turcotte, D. L., and G. Schubert (2002), *Geodynamics*, 2nd ed., 472 pp., Cambridge Univ. Press, New York, NY.

White, R. S., D. McKenzie, and R. K. O'Nions (1992), Oceanic crustal thickness from seismic measurements and rare earth element inversions, *J. Geophys. Res.*, *97*(B13), 19,683–19,715, doi:10.1029/92JB01749.

Wilson, D. S. (1993), Confidence intervals for motion and deformation of the Juan de Fuca Plate, *J. Geophys. Res.*, *98* (B9), 16,053–16,071, doi:10.1029/93JB01227.

Yang, Y., D. Forsyth, and D. S. Weeraratne (2007), Seismic attenuation near the East Pacific Rise and the origin of the low-velocity zone, *Earth Planet. Sci. Lett.*, *258*, 260–268, doi:10.10106/j.epsl.2007.03.040.

Yao, H., P. Gouédard, J. A. Collins, J. J. McGuire, and R. D. van der Hilst (2011), Structure of young East Pacific Rise lithosphere from ambient noise correlation analysis of fundamental- and higher-mode Scholte-Rayleigh waves, *C. R. Geosci.*, *343*(8–9), 571–583, doi:10.1016/j.crte.2011.04.004.